Precision Agriculture (2023) 25:681–703
https://doi.org/10.1007/s11119-023-10088-8

Mapping hailstorm damage on winter wheat (*Triticum aestivum* L.) using a microscale UAV hyperspectral approach

Jacopo Furlanetto[1] · Nicola Dal Ferro[2] · Daniele Caceffo[3] · Francesco Morari[2]

Accepted: 20 October 2023 / Published online: 11 November 2023

Abstract
Hailstorms pose a direct threat to agriculture, often causing yield losses and worsening farmers' agricultural activity. Traditional methods of hail damage estimation, conducted by insurance field inspectors, have been questioned due to their complexity, partial subjectivity, and lack of accounting for spatial variability. Therefore, remote sensing integration in the estimation process could provide a valuable aid. The focus of this study was on winter wheat (*Triticum aestivum* L.) and its response to damage in the near-infrared (NIR) spectral region, with a particular emphasis on the study of brown pigments as a proxy for yield damage estimation and mapping. An experiment was conducted during two cropping seasons (2020–2021 and 2021–2022) at two sites, simulating hail damage at critical flowering and milky stages using a specifically designed prototype machinery with low, medium, and high damage gradients compared to undamaged conditions in plots with a minimum of 400 m^2 area. After the damage simulation, hyperspectral visible-NIR reflectance was measured with Unmanned Aerial Vehicle (UAV) flights, and measurements of chlorophyll and of leaf area index (LAI) were contextually taken. Final yield per treatment was recorded using a combine. An increase in absorbance in the NIR region (780–950 nm) was observed and evaluated using a spectral mixture analysis (SMA) after selecting representative damaged and undamaged vegetation spectra to map the damage. The abundance of damaged endmember pixels per treatment resulted in a good relationship with the final yield ($R^2 = 0.73$), identifying the most damaged areas. The absorbance feature was further analysed with a newly designed multispectral index (TAI), which was tested against a selection of indices and resulted in the highest relationship with the final yield ($R^2 = 0.64$). Both approaches were effective in highlighting the absorbance feature over different dates and development stages, defining an effective mean for hailstorm damage mapping in winter wheat.

Keywords UAV · Hyperspectral · Hailstorm · Spectral mixture analysis · Brown pigments

✉ Jacopo Furlanetto
jacopo.furlanetto@phd.unipd.it

[1] TESAF dept., University of Padova, 35020 Legnaro, Padova, Italy

[2] DAFNAE dept., University of Padova, 35020 Legnaro, Padova, Italy

[3] Società Cattolica di Assicurazione S.p.A, 37126 Verona, Italy

Introduction

Extreme weather events can cause significant economic losses worldwide in the agricultural sector, with hailstorms being responsible for a considerable portion of reductions in crop yield and forage quality (de Leeuw et al., 2014; Mahul & Stutley, 2010). Defoliation, stem breakage, and direct grain loss are typical damages caused by hail in winter wheat (*Triticum aestivum* L.) (Counce et al., 1994; USDA, 2010). The degree of yield loss is mainly related to the timing of the damage event, resulting in a greater reduction during reproductive stages (Counce et al., 1994; Furlanetto et al., 2021; Zhao et al., 2012). As of now, yield loss estimates are mainly done on field by insurance inspectors, but this process has limitations such as small-scale assessment compared to the hail swath (Bell et al., 2020), strong spatial variabilities (Nisi et al., 2016), time-consuming inspections (Furlanetto et al., 2023), and a degree of subjectivity in the evaluations (Zhou et al., 2016). Optical remote sensing can help overcome these limitations and provide wide-area coverage, consistent revisit time, and repeatable measurements. Remote sensing applications from both satellites and unmanned aerial vehicles (UAVs) have been proven effective in aiding damage assessment (de Leeuw et al., 2014; Schillaci et al., 2022). Unmanned aerial vehicles (UAVs) stand out with their high ground sampling capacity (Furlanetto et al., 2023) allowing vegetation study at the microscale. They nonetheless have limitations in terms of area coverage and potential uncertainties related to variable illumination conditions (Abdelbaki et al., 2021; Zhang et al., 2021).

The optical properties of vegetation in the visible and near-infrared region (VIS-NIR) have long been recognized as a valuable tool for assessing various crop parameters, including chlorophyll (Filella & Peñuelas, 1994), leaf area index (LAI) (Fang et al., 2019), canopy water content (Peñuelas et al., 1997), and general stress/senescence (Carter, 1994; Guyot & Baret, 1988; Tucker, 1979). While these parameters may be useful for estimating hail damage in crops whose productivity loss is mainly related to defoliation, some limitations may apply when it comes to winter wheat. Defoliation is one of the most visible damages caused by hailstones on crops at the canopy level. It is often associated with yield decreases, such as in maize (Gobbo et al., 2021; Shapiro et al., 1986), although in other crops the relationship between defoliation and loss is not always linear (Lauer et al., 2004). For instance, defoliation in winter wheat has been reported to be not strictly related to yield losses, both in early (Zhu et al., 2004) and later plant development stages (Holmes, 1973). On the contrary, depending on its degree, it may not have a detrimental effect on the final yield, or, in some cases, it may even increase plant water use efficiency (Ahmadi et al., 2009). Defoliation in winter wheat can also increase the chlorophyll concentration both in the remaining leaves/leaf portions (Macedo et al., 2006) or in the inflorescence (Holmes, 1973). Although Macedo et al. (2007) found differences in the photosynthetic rate between defoliation and non-defoliation treatments, these were related to the leaf-level pattern of defoliation rather than its degree.

The microscale study of pigments other than chlorophyll may offer a feasible way to detect hail damage. Hailstones cause wounds to the leaf tissue, which leads to biochemical changes visible in dead plant portions resulting from the hail impact (Fernandes et al., 2011). For instance, when leaf tissue is disrupted and/or senescent, the polyphenol oxidase (PPO) and the polyphenols are mixed together (Vaughn & Duke, 1984), producing quinones. Quinones are often considered as a defence mechanism against herbivores, as they reduce protein assimilability and act as a physical barrier against pathogens (Mohammadi & Kazemi, 2002; Queiroz et al., 2008). Quinones are also associated with the browning

observed in wounded or senescent leaf tissue (Bittner, 2006; Queiroz et al., 2008; Richard-Forget & Goupy, 1994; Vaughn & Duke, 1984). Peñuelas et al. (2004) proposed linking quinones with the concept of brown pigments, but the definition of this latter term remains elusive. Initially included in the PROSPECT model (Jacquemoud & Baret, 1990), brown pigments were associated with the broad notion of polyphenols absorbing light at wavelengths shorter than 1300 nm (Baret & Fourty, 1997). Nonetheless, Peñuelas et al. (2004) linked them with quinones, and linked their browning feature to the PPO activity, as also suggested by Bittner (2006). This browning feature was also suggested by Richard-Forget and Goupy (1994) and Ustin and Jacquemoud (2020), and is consistent with the physiological processes described by Queiroz et al. (2008) and Vaughn and Duke (1984). However, most quinones have absorbance peaks in the UV-blue region (Bittner, 2006; Nicolas et al., 1994), while brown pigments are reported to absorb light in the NIR region. Interestingly, Pierpoint (1969) originally reported absorbance feature of certain quinones molecules in the far-red region of the spectrum.

Recently, the definition of brown pigments has been expanded to include decay pigments, which comprise a variety of compounds that appear during plant tissue decomposition and increase absorbance, particularly in the NIR region, with a peak at approximately 800 nm (Proctor et al., 2017). This unique absorbance behaviour tends to flatten the red-NIR region, making the vegetation spectrum similar to soil features. Such a physiological response seems plausible in a hail-damaged canopy, given that hailstones can defoliate and crush plant organs, compromising tissue functions and possibly leading to necrosis and activation of plant defence mechanisms (Holman et al., 2023). Moreover, Proctor et al. (2017) pointed out the high complexity of decay pigments resulting from the interaction of quinones with phenols and amino acids (Bittner, 2006; Nicolas et al., 1994), which can produce a variety of molecules that eventually affect the NIR region. This suggests that brown pigments are not directly responsible for browning but appear in brown areas as a result of cellular dismantling. Therefore, studying the effects of brown pigments on plant NIR reflectivity may provide new insights into detecting stress in winter wheat following hail damage alongside with traditional canopy level analysis (e.g., defoliation).

From this perspective, the use of hyperspectral imaging from UAV provides unprecedented insight into the reflectivity characteristics of plants at the microscale in open field situations, enabling a detailed snapshot of plant status following extreme weather events such as hailstorms. Furthermore, UAV hyperspectral data can serve as a precursor for detailed studies later to be extended to multispectral sensors, which are currently less computationally demanding, easier to use, and more commonly employed in out-of-research applications (Adão et al., 2017). The objectives of this study were to: (1) investigate winter wheat response to hail damage in the NIR region at the microscale, (2) investigate a link between the NIR changes and the damage in terms of yield drops, and (3) possibly extend the findings to applications at the multispectral level.

Materials and methods

Experimental site and design

A two-year experiment was conducted on winter wheat (*Triticum aestivum* L., var. Balneo in 2021 and Rubisko in 2022) at two different locations during the 2020–2021 and 2021–2022 cropping seasons. The first site, VL21, was located at a farm in Meolo within

the Venice Lagoon watershed (NE Italy, 45°33'20'' N, 12°25'50'' E) in 2021, while the second site, LT22, was located at the University of Padova's experimental farm "L. Toniolo" in Legnaro (45°35'01'' N, 11°94'92'' E) in 2022 (Fig. 1). VL21 has a subhumid climate with an average temperature of 14 °C and an annual rainfall of 1080 mm, with a mean reference evapotranspiration (ET_0) of 996 mm year^{-1}. The soil at VL21 is an Endogleyic Calcisol (IUSS Working Group WRB, 2015), silty-clay-loam, with low SOC (1.52 ± 0.20 g 100 g^{-1}) and low total nitrogen (0.21 ± 0.02 g 100 g^{-1}) in the tilled layer (0–30 cm). LT22 also has a subhumid climate with an average temperature of 14 °C and annual rainfall of 836 mm, with a mean reference ET_0 of 992 mm year^{-1}. The soil is a Fluvi-Calcaric Cambisol (IUSS Working Group WRB, 2015), silty-loam, with SOC and total nitrogen even lower than VL21 (SOC = 0.91 ± 0.06 g 100 g^{-1}; total N = 0.11 ± 0.01 g 100 g^{-1}) in the 0–30 cm layer (Dal Ferro et al., 2020). Agronomic field operations included a 30 cm-deep moldboard ploughing followed by seedbed preparation with a disc harrow. Fertilization was done following the crop specific requirements per site, that is 305 kg N ha^{-1} in 2021 and 178 kg N ha^{-1} in 2022.

Hail damage was simulated at both locations during both years of the experiment. A prototype specifically designed at the University of Padova was used to simulate the hail damage, consisting of a 6 m long horizontal rotating pole driven by the tractor's power take off (Fig. 2). Ropes, 0.35 m long knotted at the end, were attached to the pole and rotated at different speeds to vary the damage level. Three damage intensities were simulated, including low damage, medium damage, and high damage, respectively an estimated 20%, 50% and 80% of yield loss, which were compared with undamaged conditions (control treatment, hereafter Ctrl). Insurance field inspectors assisted in calibrating the prototype to closely resemble real hailstorm effects on crops. The damage intensity (i.e., yield loss) was evaluated based on the number of kernels that were damaged or lost, as well as leaf

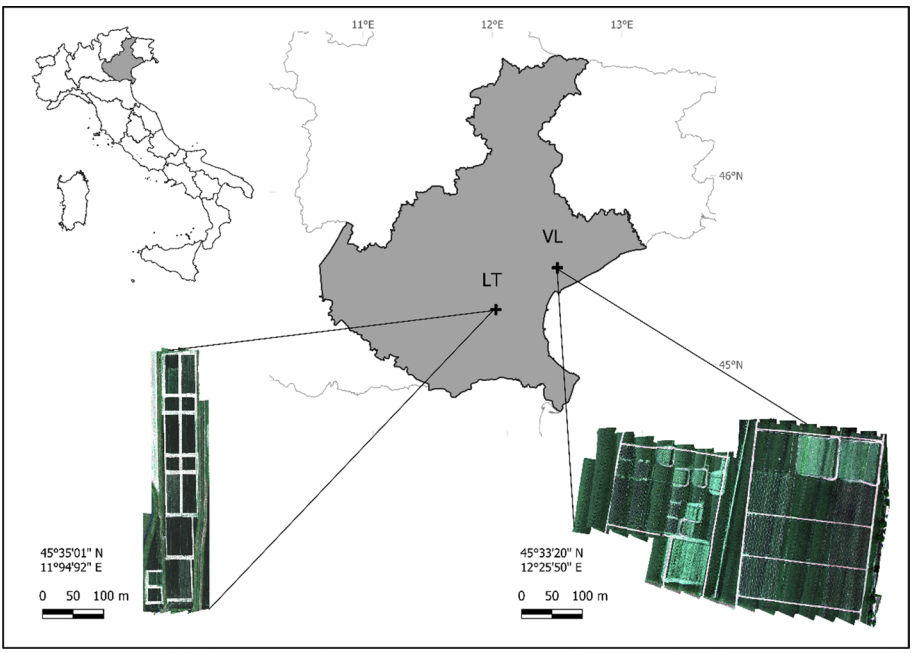

Fig. 1 Location and aerial map of the experimental sites VL (2021) and LT (2022)

Fig. 2 The designed prototype used for simulating the hail damage at different intensities during the experimentation (above). Below, detail of the rotating ropes system in action during a low damage simulation

shredding/removal and stem breakage. The prototype rotating speed was therefore adjusted to achieve the planned 20%, 50% and 80% yield losses.

Treatments were performed during two different plant development stages: flowering (F) and milky (M), according to the BBCH phenological scale, BBCH 61–69 and BBCH 75 (Lorenz et al., 2001), respectively. In 2021, damages were simulated on May 18th (F) and May 31st -June 3rd (M), while in 2022, treatments were done on May 11th (F) and May 26th (M). Treatments were performed in triplicate in plots measuring either 20×20 m or 60×60 m at VL21 and 20×20 m at LT22. The large plot size at VL21 derived from their inclusion in a wider experimentation, which also included satellite imagery whose image resolution was lower than that of UAV. No natural hailstorm events occurred over the sites during the experiment.

Ground measurements

Chlorophyll and LAI measurements were conducted 7–10 days after damage was inflicted to the crops. This allowed the plants to fully exhibit their morphological and physiological responses (such as leaf drying and necrosis). Four points per plot were sampled, with three

replicates per point, along with remote measurements. Chlorophyll was measured on the flag leaf using a DUALEX active handheld optical pigment detector (FORCE-A, Orsay, France). The LAI was measured from mid-morning to mid-afternoon on clear-sky days using an Accupar LP-80 (Decagon Devices Inc., Pullman, WA, USA). To minimize the effect of accidental movements (Pokovai & Fodor, 2019), each reading was calculated as an average of five individual measurements taken in different probe positions, scanning an area of approximately 1 m^2.

Yield measurements were obtained using a CX 5090 combine (New Holland, Torino, Italy) equipped with a yield monitor and a differential global positioning system. The combine was calibrated after measuring a "ground truth" load weight at a weigh station. Raw yield data were then cleaned to exclude field-edge effects and harvester manoeuvres using the methodology described in Ping and Dobermann (2005). Yield data were expressed as grain dry matter per hectare (t DM ha^{-1}).

Remote sensing monitoring

Unmanned Aerial Vehicle (UAV) flights were performed over the experimental plots after each damage simulation, using a Matrice 600 Pro drone (DJI, Shenzhen, China). The UAV was equipped with a nanoHyperspec hyperspectral camera (Headwall Photonics, Bolton, MA, USA) mounting a 12 mm lens and stabilized with a Ronin MX Gimbal system (DJI, Shenzhen, China). The camera works as a push and broom sensor recording 640×n pixels images. It detects incoming radiation in the 400–1000 nm range, with a FWHM of 6.6 nm and a dispersion/pixel of 2.2 nm resulting in 273 bands. In 2021 flight height was 70 m -ground sample distance (GSD) of 4.4 cm-, while in 2022 it was 50 m -GSD of 3.5 cm-. Flights were completed between 11 a.m. and 15 p.m. on clear sky days. Prior to each flight a dark reference image was acquired, accounting for the camera self-noise. Two reference reflectance calibration tarps (Group 8 Technology, Provo, UT, USA) were placed on the scene, plainly visible to the sensor and free from shadows.

Hyperspectral image elaboration

Hyperspectral image pre-processing and processing steps were conducted as described by Adão et al. (2017), with few changes described below. The images were pre-processed and orthorectified using the SpectralView software (Headwall Photonics, Bolton, MA, USA). The pre-processing of the full recorded spectrum included non-uniformity correction, conversion to radiance, conversion to reflectance, and orthorectification of the single flight swaths. A mean white reference spectrum was selected for each image using the Spectral Angle Mapper (SAM) classification tool included in the software. The classification was based on a manually selected pure white pixel over the calibration tarp. Subsequent image processing steps were completed while keeping the single flight swaths separated, avoiding the merging of overlapping areas wherever possible. This made it possible to work on "pure pixels" at all stages, thus avoiding spectral resampling in imperfectly overlapping pixels between swaths that would have resulted in raw spectral contamination. The final output was merged to create a full map. The spectra were smoothed using a Savitzky-Golay filter (window size = 11, polynomial order = 3) as implemented in the QGIS EnMAP-Box Plugin (EnMAP-Box Developers, 2019) to reduce signal noise while preserving the full spectral resolution.

Linear spectral unmixing

Linear spectral mixture analysis (SMA) was performed using the ENVI software (Exelis Visual Information Solutions, Boulder, CO, USA) to monitor the effect of simulated hailstorm on winter wheat tissues. This technique proved to be effective to describe vegetation reflectance from remote sensing multispectral and hyperspectral imagery in every pixel described as combinations of different factors called spectral endmembers (e.g., Dawelbait et al. (2017); Yuan et al. (2021)). Two endmembers were selected, i.e., damaged and undamaged vegetation. The endmembers were selected on the LT22-19/05 image and used for classification on the three other dates as well. The selection focused on the distinctive features in the 780–950 nm range, opting for spectra that differed mostly on that region. Endmembers were selected using a hybrid method based on principal component discrimination and image visual inspection. A number of ten spectra was selected as representative, and these were averaged to obtain a final reference endmember. The undamaged vegetation endmember was selected on undamaged plots, while the damaged endmember was selected among the damage treatment plots, thus well identifying damaged vegetation and minimizing the incidence of undamaged vegetation features. The image analysis was conducted at the native image resolution and only on pixels fully representing vegetation, meaning that areas including bare soil and tractor prints caused during the damage simulation were masked out and not included in the analysis.

Definition of the newly proposed index

A new index aimed at detecting changes in the NIR region (i.e., brown pigments) was designed and named TAI (Triangular Area Index). The TAI is therefore a simple and easy to apply geometric index defining the triangular area constrained between the near-infrared (NIR) and the red-edge (RE) regions. The general formulation is as follows:

$$TAI = \frac{\left(\rho_{NIR-}\rho_{RE}\right) \times (NIR_{CW} - RE_{CW})}{2} \quad (1)$$

where ρ_{NIR} is the reflectance value of the NIR band, ρ_{RE} is the reflectance value of the RE band, NIR_{CW} and RE_{CW} are the corresponding central wavelengths. The used central wavelengths were 865 nm (NIR) and 783 nm (RE), with a bandwidth comparable with the MSI Sentinel-2 (approximately 20 nm). The index value increases as the difference in reflectance between 865 nm and 783 nm increases, while it approaches the zero value the flatter the NIR region is. A visual representation of the index is reported in Fig. 3.

Stress indices considered in the study

Six other stress indices were also considered in this study (Table 1). They were selected after scrutiny of suitable indices addressing comparable plant physiological responses as of this study and focusing on similar spectral features. Among the indices, BPI (Brown Pigment Index) (Peñuelas et al., 2004) stands out for its design meant at capturing brown pigment presence in green vegetation. Its computation relies on the second derivative of the spectrum, calculated according to the indications provided by Rinnan et al. (2009), using a

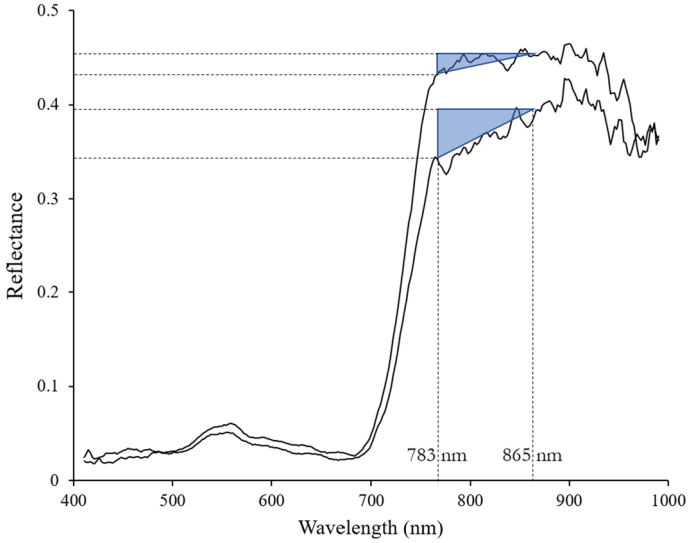

Fig. 3 Visual representation of the TAI in case of an undamaged (upper) and damaged (lower) spectrum

Table 1 Selected indices used in the study and respective formulation and references

Index	Formula	References
BPI	Wavelength difference where 2nd derivative crosses 0 in the NIR and far-red regions	(Peñuelas et al., 2004)
Carter2	$\frac{\rho_{698\sim694}}{\rho_{762\sim758}}$	(Carter, 1994)
NDVI	$\frac{\rho_{875\sim855}-\rho_{680\sim650}}{\rho_{875\sim855}+\rho_{680\sim650}}$	(Tucker, 1979)
PSRI	$\frac{\rho_{683\sim678}-\rho_{503\sim499}}{\rho_{753\sim749}}$	(Merzlyak et al., 1999)
REIP	$740 \times \frac{\frac{\rho_{672\sim667}+\rho_{782\sim778}}{2}-\rho_{702\sim698}}{\rho_{742\sim738}-\rho_{702\sim698}}$	(Guyot & Baret, 1988)
TAI	$\frac{(\rho_{875\sim855}-\rho_{793\sim773})\times(865-783)}{2}$	This study
TTVI	$0.5 \times (783-740) \times \left(\rho_{875\sim855}-\rho_{742\sim738}\right)-(865-740) \times (\rho_{793\sim773}-\rho_{742\sim738})$	(Xing et al., 2020)

Savitzky-Golay filter aimed at smoothing the second derivative to reduce its noise-enhancing behaviour.

Results

Weather

The mean temperature remained relatively stable during the winter and early spring between the two years. However, during late spring and early summer of 2022, the

Table 2 Weather data for the two sites at Venice Lagoon Watershed 2021 (VL21) and Padova 2022 (LT22) for the winter wheat season from seeding to harvesting (November–July)

	VL21		LT22	
	Mean T (°C)	Precipitation (mm)	Mean T (°C)	Precipitation (mm)
Nov	10.6	199.0	9.3	95.2
Dec	6.0	98.6	3.9	36.2
Jan	3.0	87.6	3.0	20.4
Feb	7.0	30.8	6.2	10.2
Mar	8.1	6.6	8.2	13.8
Apr	11.5	114.2	12.0	39.8
May	15.8	142.0	20.0	32.8
June	23.8	45.4	24.5	11.0
July	24.6	0.6	26.2	32.0
	Total	724.8	Total	291.4

temperature was higher than that of 2021, as shown in Table 2. In particular, the average monthly temperature in May 2022 was 4.2 °C higher than in 2021. Precipitation was notably low during winter-spring 2022, with a relative difference of − 77 and − 76% observed during the flowering and milky stages in May and June 2022 compared to 2021. The total precipitation recorded was 724.8 mm in VL21 and 291.4 mm in LT22, as shown in Table 2.

Ground measurements

Chlorophyll content exhibited mixed behaviour following damage, with visible differences observed between the two sites (Table 3). Specifically, little to no differences were observed in VL21, where damage treatments often resulted in higher chlorophyll content than the control, particularly in F-medium damage in VL21-09/06. In contrast, in LT22, chlorophyll content exhibited lower values in the damage treatments at all dates. This behaviour did not strictly follow damage intensity, often leading to larger chlorophyll decreases in lower damage levels. LAI measurements in both VL21 and LT22 often showed little to no difference compared to Ctrl (Table 3). Generally lower values were observed as damage increased in LT22-19/05 survey. However, these results were not similarly found during the survey conducted on LT22-08/06, when the high damaged plots did not show the greatest LAI reduction compared to other less intense damages.

The hail damage treatments caused a significant reduction ($p < 0.05$) in wheat yield compared to undamaged plots at both VL21 and LT22. The average yield in Ctrl was 7.41 t ha^{-1} in VL21 and 7.44 t ha^{-1} in LT22. As damage intensity increased, the yield decreased accordingly, consistently with a negative gradient (Table 4). In particular, VL21 exhibited a significant difference among treatments, revealing a strong negative correlation between the level of damage and yield. The highest level of damage in the milky stage (M) resulted in a peak loss of 69%. Conversely, in LT22, only the control exhibited a significant difference from the other treatments, despite an observed negative trend in line with the level of damage (Table 4).

Table 3 Chlorophyll content and LAI measured on field for the two sites of VL21 and LT22

Year and site	Stage of damage	Treatment	Chlorophyll (μg cm^{-2})	Δ%[a]	LAI	Δ%[a]
VL21-20/05	F	Ctrl	29.71± 1.85		5.28± 0.20	
		Low	30.81± 0.27	3.7	5.64± 0.35	6.8
		Me	29.12± 1.93	− 2.0	5.11± 0.27	− 3.2
		Hi	30.57± 1.47	2.9	5.34± 0.40	1.1
VL21-09/06		Ctrl	31.08± 3.01		4.56± 0.21	
	F	Low	32.24± 2.51	3.7	4.94± 0.10	8.3
		Me	35.08± 3.31	12.9	4.72± 0.13	3.5
		Hi	32.03± 2.02	3.1	4.75± 0.17	4.2
	M	Low	32.51± 0.49	4.6	4.53± 0.17	− 0.7
		Me	30.10± 1.19	− 3.2	4.46± 0.44	− 2.2
		Hi	29.64± 2.64	− 4.6	4.30± 0.26	− 5.7
LT22-19/05		Ctrl	47.36± 0.45		6.02± 0.45	
	F	Low	42.68± 0.53	− 9.9	5.47± 0.53	− 9.1
		Me	40.95± 0.43	− 13.5	5.29± 0.43	− 12.1
		Hi	41.88± 0.50	− 11.6	5.14± 0.50	− 14.6
LT22-08/06		Ctrl	35.49± 0.42 (a)		4.62± 0.42	
	F	Low	23.86± 0.46 (b)	− 32.8	4.46± 0.46	− 3.5
		Me	26.15± 0.30 (b)	− 26.3	4.69± 0.30	1.5
		Hi	27.61± 0.31 (ab)	− 22.2	4.53± 0.31	− 1.9
	M	Low	29.37± 0.44 (ab)	− 17.2	4.40± 0.44	− 4.8
		Me	32.07± 0.12 (ab)	− 9.6	4.11± 0.12	− 11.0
		Hi	27.96± 0.25 (ab)	− 21.2	4.17± 0.25	− 9.7

[a]Δ%: percentage variation of each damaged treatment compared with the control treatment

Post-hoc Tukey test letters of significance are reported (α = 0.05)

Table 4 Yield outputs per treatment at the two experimental sites VL21 and LT22. Post-hoc Tukey test letters of significance are reported (α = 0.05)

Year and site	Stage of damage	Treatment	Yield (t ha^{-1})	Δ% with Ctrl
VL21		Ctrl	7.41± 0.08 (a)	
	F	Low	5.50± 0.30 (b)	− 25.8
		Me	4.28± 0.32 (bc)	− 42.2
		Hi	3.17± 0.12 (cde)	− 57.2
	M	Low	4.12± 0.58 (bd)	− 44.4
		Me	3.04± 0.46 (cde)	− 59.0
		Hi	2.29± 0.48 (e)	− 69.1
LT22		Ctrl	7.44± 0.35 (a)	
	F	Low	4.11± 0.41 (b)	− 44.8
		Me	3.78± 0.32 (b)	− 49.2
		Hi	3.37± 0.24 (b)	− 54.7
	M	Low	4.62± 0.17 (b)	− 37.9
		Me	4.48± 0.28 (b)	− 39.8
		Hi	3.99± 0.07 (b)	− 46.4

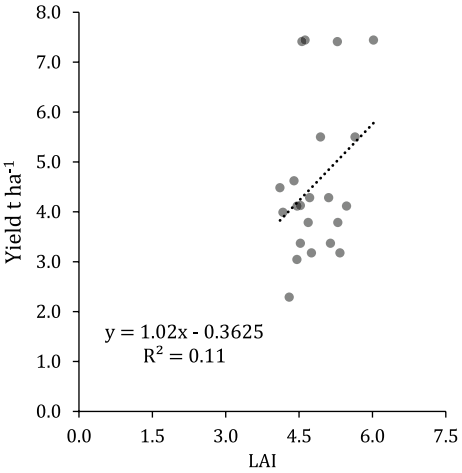

Fig. 4 Regression between yield and LAI including both sites VL21 and LT22

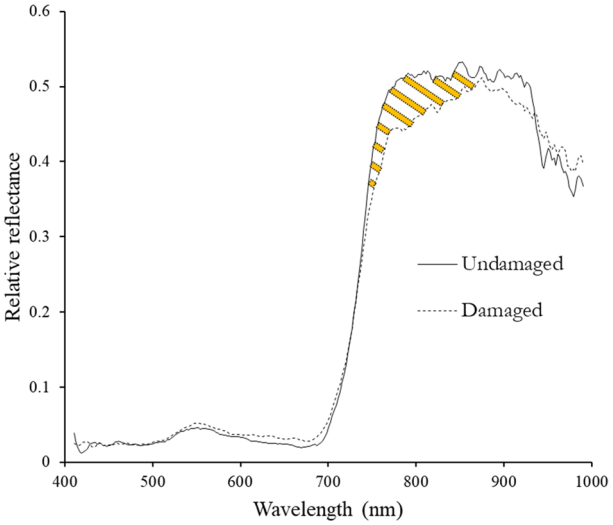

Fig. 5 Selected spectra endmembers for undamaged and damaged winter wheat plants. The area with strips indicates the object of the study, the NIR shoulder reflectance dissimilarity between the two

Yield and LAI showed a poor correlation (not significant) in both VL21 and LT22 ($R^2 = 0.11$) (Fig. 4). Yield differences between damage levels were hardly captured by LAI, remarking its lack of differentiation between treatments reported in Table 3.

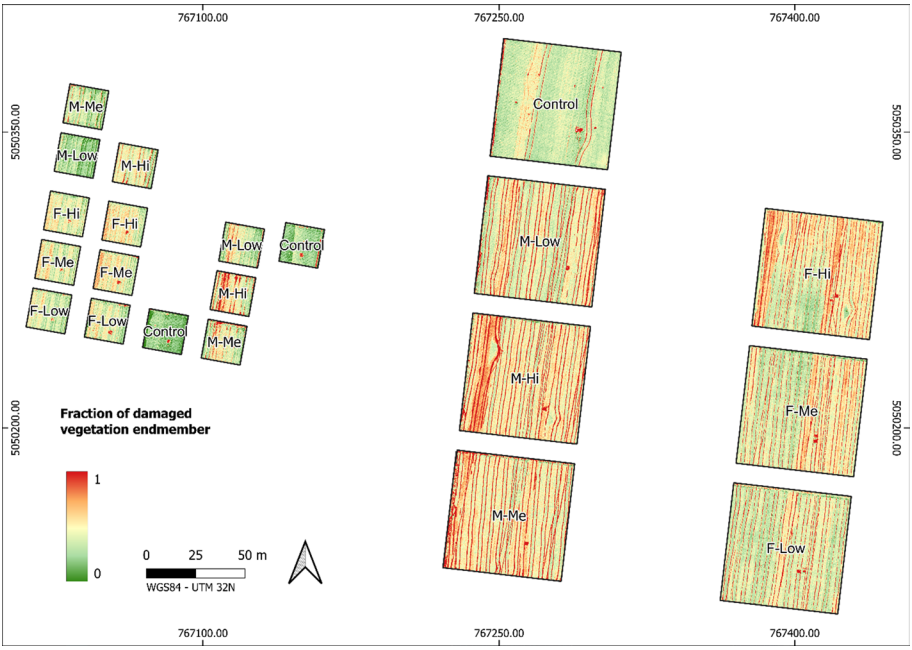

Fig. 6 Linear spectral unmixing results from the VL experimental field on June 9th, 2021. The colour gradient ranges from 0 (0% abundance of damaged spectrum in the pixel) to 1 (100% abundance of damaged spectrum in the pixel). Red straight lines in between plots (value = 1) represent tractor tire prints, thus completely dead vegetation (Color figure online)

Endmembers definition

Two average representative spectra were selected as endmembers for wheat, that is undamaged and damaged (Fig. 5). A different pattern is clear in the NIR-shoulder region, approximately from 760 to 950 nm, where damaged relative reflectance was −9% on average compared to the undamaged spectra. The highest difference (− 15%) was observed at 760 nm, while the lowest (− 2%) at 868 nm.

Spectral unmixing

The spectral unmixing technique was effective in distinguishing between damaged and undamaged plots, and in mapping the hail damage level in both VL21 and LT22. As an example, the classified map of VL21-09/06 (Fig. 6) clearly differentiated between damaged and undamaged areas. Control plots were also clearly distinguishable from the other treatments, which had damaged endmember abundance ranging from 0 to 30%. Notably, also control plots showed some slight degree of damaged endmember presence as well, particularly in the larger 60 × 60 m plot. Treatment plots that were damaged during the flowering (F) and milky (M) stages showed an increasing abundance of the damaged endmember as the damage intensity increased, as well as intra-plot variability.

Table 5 Percentage of pixels with damaged endmember abundance above a specific threshold (50–90%), per treatment. Data is reported for each sampling date and for each site

Sampling date	Stage of damage	Treatment	Damaged endmember fraction (% of pixels) above abundance threshold				
			50%	60%	70%	80%	90%
20/05/2021	F	Ctrl	13.7 ± 2.5	8.7 ± 1.8	5.3 ± 1.2	3.2 ± 5.6	2 ± 3.5
		Low	22.6 ± 7	14.4 ± 4.6	8.6 ± 2.8	4.9 ± 8.5	2.6 ± 4.4
		Me	32.2 ± 8.6	21.3 ± 5.9	13.1 ± 3.6	7.6 ± 13.1	4.1 ± 7
		Hi	37.1 ± 7.9	25.1 ± 5.6	16 ± 3.7	9.4 ± 16.3	5 ± 8.7
09/06/2021		Ctrl	21.4 ± 7.6	13.4 ± 5.1	7.9 ± 3.1	4.5 ± 7.9	2.7 ± 4.6
	F	Low	34.9 ± 4	23.6 ± 3.3	15 ± 2.4	9.1 ± 15.8	5.5 ± 9.5
		Me	41.1 ± 3.1	29.2 ± 2.8	19.4 ± 2.3	12.3 ± 21.3	7.7 ± 13.3
		Hi	47.5 ± 7.7	35.7 ± 7.5	24.6 ± 6.1	15.5 ± 26.9	9.2 ± 15.9
	M	Low	33.8 ± 10.2	24.2 ± 8.4	16.6 ± 6.5	11.3 ± 19.5	7.6 ± 13.2
		Me	41.4 ± 10.1	30.9 ± 8.9	21.6 ± 7.1	14.7 ± 25.5	10 ± 17.2
		Hi	48.6 ± 7.3	38.1 ± 6.9	28.4 ± 6.1	20.4 ± 35.3	14.4 ± 24.9
19/05/2022		Ctrl	3.6 ± 0.6	1.9 ± 0.3	0.8 ± 0.1	0.4 ± 0.7	0.2 ± 0.3
	F	Low	22 ± 8.3	13.7 ± 6	6.7 ± 3.3	4.7 ± 8.1	2.1 ± 3.7
		Me	29.7 ± 2.9	18.5 ± 2.3	9 ± 1.4	6 ± 10.5	2.7 ± 4.6
		Hi	38.4 ± 7.5	25.7 ± 6.5	13.3 ± 4.2	9.5 ± 16.4	4.5 ± 7.7
08/06/2022		Ctrl	15 ± 2	8.3 ± 1.1	4.1 ± 0.6	1.8 ± 3.1	0.7 ± 1.3
	F	Low	25.9 ± 5.1	15.5 ± 3.5	8.5 ± 2.3	4.1 ± 7	1.8 ± 3.1
		Me	22.6 ± 3.3	13.2 ± 2.3	6.9 ± 1.5	3.4 ± 5.8	1.5 ± 2.6
		Hi	24.1 ± 3.9	14.2 ± 2.7	7.7 ± 1.7	3.7 ± 6.4	1.6 ± 2.8
	M	Low	24.4 ± 5.2	14.4 ± 3.5	7.9 ± 2.2	4 ± 6.9	1.9 ± 3.2
		Me	37.3 ± 9.6	23.7 ± 6.8	13.8 ± 4.5	7.4 ± 12.9	3.8 ± 6.5
		Hi	32.6 ± 7.2	20.5 ± 5	11.9 ± 3.1	6.4 ± 11	3.1 ± 5.4

When analyzing the normalized percentage of pixels per treatment that exceeded increasing damaged spectrum abundance thresholds (Table 5), a clear gradient was observed. For this analysis, tractor prints (Fig. 6) and visible soil were masked out. VL21-20/05 and LT22-19/05 exhibited comparable values of damaged spectrum pixels during the flowering stage, across all thresholds. For instance, when considering the 50% threshold, the differences in percentage points between VL21-20/05 and LT22-19/05 were only 0.6, 2.5, and − 6.1% respectively, in low, medium, and high damages during the flowering stage. Nevertheless, a higher difference was observed between the control treatments, up to 10.1%. In June, the agreement between the two sites was less consistent. The difference between the abundance of damaged spectrum pixels in plots damaged during the flowering and milky stages was larger, ranging from 4.1% in milky (medium damage) to 23.3% in flowering (high damage). Notably, LT22-08/06 showed a lack of response to the damage level across all selected thresholds, not following a clear gradient in the plots damaged during flowering (lower > higher) and during milky (medium > higher). However, all damage treatments yielded a higher abundance of the damaged feature at all thresholds compared to the control.

A strong relationship between yield and the 50% damaged endmember abundance threshold was observed, with the exception of LT22-08/06, as shown in Table 6. The

Table 6 R^2 coefficients between yield and pixel frequency (in %) with damaged endmember fraction above the threshold

Sampling date	% of pixels with damaged endmember fraction above threshold				
	50%	60%	70%	80%	90%
VL21-20/05	0.99	0.98	0.97	0.96	0.92
VL21-09/06	0.87	0.91	0.93	0.93	0.90
LT22-19/05	0.91	0.88	0.86	0.84	0.82
LT22-08/06	0.29	0.27	0.24	0.21	0.17
Overall	0.60	0.55	0.45	0.43	0.33
Overall (no LT22-08/06)	0.73	0.71	0.60	0.63	0.50

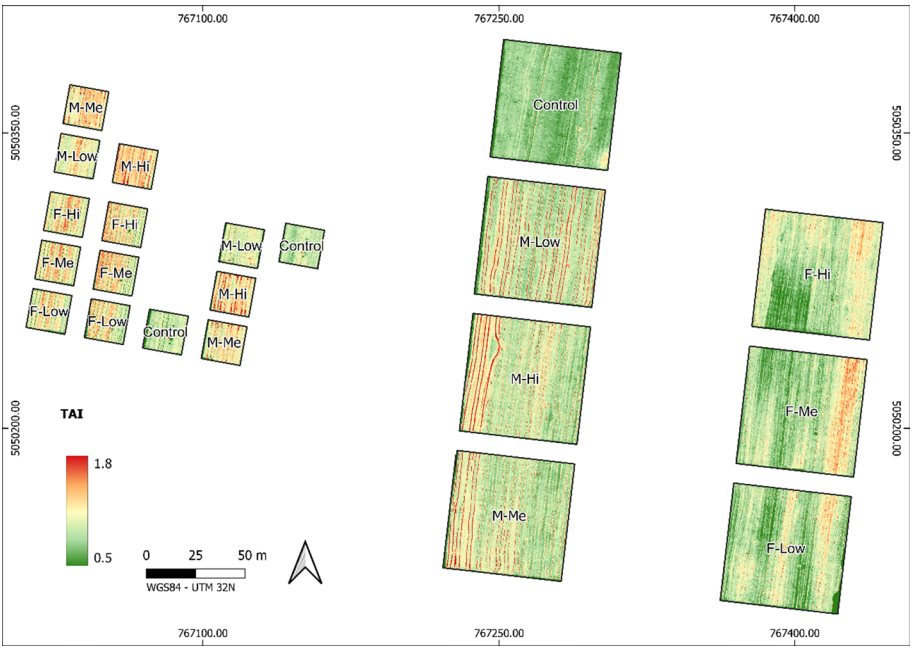

Fig. 7 Map of TAI index over VL21 site on June 9th, 2021. Labels in the plot refer to the control and simulated hailstorm event intensity and period of occurrence

highest R^2 values were obtained using the 50% threshold for VL21-20/05, and 70% and 80% for VL21-09/06. For both LT22-19/05 and LT22-08/06, the 50% threshold also resulted in high R^2 values. Overall, the 50% threshold was the most strongly related with yield, with an R^2 value of 0.60. When excluding LT22-08/06, this relationship was improved, with an R^2 value of 0.73, highlighting its distinct response and lack of discrimination between damage levels (as described in Table 5). The R^2 values decreased noticeably when more selective abundance thresholds were applied in all cases.

Fig. 8 Map of NDVI index over VL21 site on June 9th, 2021. Labels in the plot refer to the control and simulated hailstorm event intensity and period of occurrence

Multispectral indices

The capability of different indices to map the damage varied, as indicated by the differences observed when comparing the maps generated using the newly designed TAI with NDVI (see Figs. 7 and 8). The TAI was able to detect local scale differences not only between control and damaged plots but also within individual plots (see Fig. 7), often corresponding to the SMA maps (see Fig. 6). The index demonstrated greater sensitivity to subtle changes in the vegetation response in the NIR shoulder region. In contrast, NDVI exhibited relatively homogenous mapping results, detecting fewer differences between treatments, mostly noticeable in the flowering damaged plots (Fig. 8). Moreover, little to no variability was observed within single plots.

The newly designed TAI effectively captured the damage gradient across all dates and experimental fields, with the exception of LT22-08/06. In VL21-19/05, TAI ranged from 0.47 in the control to 1.03 in higher damage (Table 7). Subsequent analysis conducted in June (VL21-09/06) reported comparable values in the flowering-damaged plots, while the control almost doubled. In VL21-09/06, the milky damaged plots ranged from 0.89 to 1.20. A similar trend was observed in LT22-19/05, albeit with lower differences between damage treatments. Nevertheless, TAI showed higher variability compared to the other indices, especially when compared to NDVI, particularly at the VL21 site. A stronger average NDVI gradient was observed only in LT22. Particularly on LT22-19/05, a clear difference between the undamaged and the higher damage treatment (0.91 vs. 0.84) appeared, with a consistent gradient between damage levels. Such a pattern was less clear on LT22-08/06, notably leading to higher NDVI values in high damage flowering plots compared to the

Table 7 Indices values per treatment at the two sites of VL21 and LT22

Sampling date	Stage of damage	Treatment	TAI	NDVI	REIP	TTVI	Carter2	PSRI	BPI
VL21-20/05	F	Ctrl	0.47 ± 0.16	0.89 ± 0.01	731 ± 0.00	− 6.20 ± 0.24	0.09 ± 0.00	− 0.010 ± 0.000	82.53 ± 0.19
		Low	0.82 ± 0.14	0.88 ± 0.01	730 ± 0.67	− 6.27 ± 0.60	0.09 ± 0.01	− 0.010 ± 0.000	82.40 ± 0.23
		Me	0.96 ± 0.18	0.88 ± 0.00	730 ± 0.67	− 6.06 ± 0.60	0.10 ± 0.01	− 0.010 ± 0.000	82.38 ± 0.24
		Hi	1.03 ± 0.19	0.88 ± 0.00	729 ± 0.67	− 5.57 ± 0.61	0.10 ± 0.01	− 0.010 ± 0.000	82.31 ± 0.20
VL21– 09/06		Ctrl	0.89 ± 0.09	0.81 ± 0.01	726 ± 0.33	− 4.26 ± 0.20	0.17 ± 0.01	0.011 ± 0.001	93.76 ± 1.73
	F	Low	1.10 ± 0.10	0.80 ± 0.01	726 ± 0.33	− 3.58 ± 0.06	0.18 ± 0.01	0.015 ± 0.001	94.69 ± 2.34
		Me	1.17 ± 0.13	0.79 ± 0.01	726 ± 0.33	− 3.43 ± 0.01	0.18 ± 0.01	0.018 ± 0.001	95.20 ± 2.98
		Hi	1.17 ± 0.14	0.79 ± 0.01	726 ± 0.33	− 3.26 ± 0.02	0.18 ± 0.01	0.019 ± 0.002	95.85 ± 3.84
	M	Low	1.03 ± 0.08	0.80 ± 0.01	726 ± 0.33	− 4.09 ± 0.09	0.17 ± 0.01	0.014 ± 0.002	95.53 ± 3.02
		Me	1.15 ± 0.10	0.81 ± 0.01	727 ± 0.33	− 4.11 ± 0.04	0.16 ± 0.01	0.015 ± 0.002	97.24 ± 4.30
		Hi	1.20 ± 0.11	0.80 ± 0.01	726 ± 0.33	− 3.86 ± 0.09	0.17 ± 0.01	0.017 ± 0.001	97.17 ± 4.49
LT22– 19/05		Ctrl	0.81 ± 0.07	0.91 ± 0.00	733 ± 0.33	− 6.62 ± 0.35	0.08 ± 0.00	− 0.007 ± 0.001	83.66 ± 0.62
	F	Low	1.03 ± 0.02	0.87 ± 0.02	731 ± 0.33	− 5.93 ± 0.40	0.11 ± 0.01	0.003 ± 0.003	80.66 ± 0.39
		Me	1.06 ± 0.07	0.85 ± 0.01	730 ± 0.88	− 5.49 ± 0.33	0.12 ± 0.01	0.005 ± 0.001	80.44 ± 0.31
		Hi	1.06 ± 0.09	0.84 ± 0.01	730 ± 1.20	− 5.29 ± 0.49	0.13 ± 0.01	0.005 ± 0.002	80.99 ± 0.44
LT22– 08/06		Ctrl	1.19 ± 0.14	0.69 ± 0.02	734 ± 0.67	− 3.53 ± 0.32	0.22 ± 0.01	0.013 ± 0.002	89.40 ± 0.39
	F	Low	1.32 ± 0.08	0.62 ± 0.07	732 ± 1.76	− 2.42 ± 0.53	0.30 ± 0.08	0.015 ± 0.001	89.36 ± 0.40
		Me	1.13 ± 0.08	0.67 ± 0.02	733 ± 0.88	− 2.65 ± 0.17	0.23 ± 0.02	0.016 ± 0.001	89.63 ± 0.18
		Hi	1.03 ± 0.07	0.66 ± 0.03	733 ± 0.88	− 2.81 ± 0.25	0.24 ± 0.03	0.015 ± 0.000	89.13 ± 0.29
	M	Low	1.38 ± 0.09	0.67 ± 0.03	733 ± 1.15	− 2.95 ± 0.41	0.24 ± 0.03	0.016 ± 0.001	89.22 ± 0.20
		Me	1.40 ± 0.06	0.64 ± 0.01	732 ± 0.33	− 2.61 ± 0.11	0.27 ± 0.02	0.019 ± 0.002	89.45 ± 0.14
		Hi	1.26 ± 0.09	0.66 ± 0.01	733 ± 0.33	− 2.95 ± 0.03	0.25 ± 0.01	0.018 ± 0.001	88.89 ± 0.28

lower damage treatments. A similar lack of differentiation was observed for the milky damaged plots. The red-edge inflection point (REIP) index only slightly captured average differences between the damage levels at all sites and dates. REIP only highlighted differences between the control and the damages, with the exception of VL21-09/06. TTVI, a geometric index like TAI, was similarly able to capture an average gradient across the experiments, with the notable exception of VL21-20/05, where no clear pattern was visible. It particularly discriminated between damage and non-damaged and within damage in VL21-09/06, where a clear gradient was observed. Carter2 highlighted average gradients mostly on VL21-20/05 and on LT22-19/05 but led to weaker differences in both VL21-09/06 and LT22-08/06. No differentiation was highlighted by PSRI in VL21-20/05, while generally lower values were observed for Ctrl in VL21-09/06 and LT22-08/06, where a gradient following damage intensity was generally present. The BPI yielded little to no average gradient in all examined dates but LT22-19/05. Moreover, in VL21-09/06 the BPI showed a relatively higher amount of variability compared to the other dates. Notably, all tested indices showed a weaker capability in capturing the damage gradient on LT22-08/06, often resulting in an inverse trend following damage and on uneven results compared to the previous observations. In most cases, higher damage plots in both flowering and milky treatments showed less apparent stress conditions than lower damage or control on this date.

The UAV hyperspectral-derived indices were finally used in a regression analysis to evaluate the explained yield variability (Table 8). Generally, a poor relationship between indices and yield across all sites and dates was found, with the exception of TAI. In fact, TAI was the only index that was able to explain some yield variability, even if lower than 30%. In contrast, all other indices were not able to capture the yield variability as affected by hail damage. Strong increase in the explained yield variability was found when data from LT22-08/06 were excluded from the analysis. In fact, a strong differentiation in crop reflectance behaviour in late season 2022 was observed compared to the previous one and from other survey dates, that was due to extraordinary dry conditions (Table 2). Nevertheless, the indices from the literature were still far from the explained variability of the TAI, which was able to capture 64% of yield variability between sites and dates, excluded LT22-08/06 ($R^2 = 0.64$). It follows that indices generally failed to capture the variability between the different sites, dates and phenological stages concerning hail damage, apart for TAI.

Discussion

Spectral mixture analysis is commonly used in satellite imagery, whereas its application in UAV systems has so far not been widely used, given the already high specificity of reflectance at the centimetre-level resolution. However, even at such micro-scale, pixel mixture is present (Sankey et al., 2017), and the integration of this technique in crop yield prediction has been shown to improve estimates (Yuan et al., 2021). Our study highlights the robustness of spectral mixture analysis through the endmember selection method. Endmembers were indeed selected on LT22-19/05 and applied to all other surveys. The classification was consistent over two years and sites, demonstrating the method sensitivity in mapping stressed vegetation at the micro-scale and responding to an increasing abundance of the damaged spectrum feature, i.e., a pronounced increase in absorbance between 780 and 950 nm.

Despite this effectiveness, LT22-08/06 showed little to no differentiation in the damaged spectrum abundance between treatments, and particularly between control and damages.

Table 8 Regression coefficients (slope, a; intercept, b) and coefficients of determination (R^2) of linear equation models between UAV hyperspectral-derived indices and yield. The linear models were applied either including or excluding LT-June, highlighting the variability introduced

		TAI	NDVI	REIP	TTVI	Carter2	PSRI	BPI
With LT-08/06	Param	a = − 0.0690	a = − 0.0254	a = 0.4135	a = − 0.2679	a = − 0.0087	a = 0.0024	a = 0.6796
		b = 1.3923	b = 0.4974	b = 728.42	b = − 3.0435	b = 0.2119	b = 0.0192	b = 91.742
	R^2	0.27	0.03	0.05	0.09	0.04	0.11	0.03
Without LT-08/06	Param	a = − 0.0898	a = 0.0103	a = − 0.444	a = − 0.2699	a = − 0.008	a = 0.0027	a = 0.8683
		b = 1.4103	b = 0.7927	b = 726.91	b = − 3.6948	b = 0.1715	b = 0.0174	b = 92.309
	R^2	0.64	0.17	0.10	0.15	0.13	0.16	0.04

This behaviour raised questions about the suitable time and conditions for a red-NIR analysis based on the brown pigments concept. As suggested by Proctor et al. (2017), brown pigments could be broadly defined as decay pigments, which are reported to naturally increase in senescent vegetation (brown areas). The LT22-08/06 survey occurred shortly after the milky stage, nonetheless it showed visible signs of senescence, i.e., yellowing/browning. This behaviour was not observed to such an extent in VL21-09/06, as also highlighted by the better classification performance observed in the latter. This discrepancy is possibly the result of the different amount of precipitation between the two years, with 2022 resulting in − 84% of precipitation volume during the critical months of April, May and June over the two sites. This could have accelerated the senescence process in winter wheat (Stasik et al., 2020), thus masking the effect of the hail damage and levelling the amount of brown pigments between treatments. Moreover, lower NDVI and slightly higher PSRI values were found on LT22-08/06 compared to VL21-09/06, possibly indicating an advanced senescing stage.

As pointed out by Adão et al. (2017), the implementation of hyperspectral data and analysis outside of research settings, or in cases of technical/economic constraints, may currently be challenging. Additionally, although SMA seems effective, prior endmember selection may lead to inconsistency or arbitrary decisions. Therefore, multispectral indices approaches are a viable option to overcome these limitations. In this study, most of the tested indices exhibited low relationship with the final yield, especially when LT22-08/06 was included. This variability may be due to differences in precipitation, soil characteristics, and management practices between the two sites. Regressions between indices and yield at the LT22-08/06 site behaved similarly to SMA, supporting the hypothesis that a lack of precipitation and early senescence may hinder analysis. Thus, an approach incorporating information from various sources, such as weather stations and different indices, could aid in selecting suitable time windows for damage assessment. This may be particularly critical since flowering and milky stages proved effective in assessing hail damage and are among the most sensitive stages in rainfed wheat conditions (Holman et al., 2023), but offer a relatively short time frame for analysis before winter wheat naturally becomes senescent.

Overall, the TAI index proposed in this study demonstrated the most stable performance across both sites and appeared to be less affected by site-specific conditions influencing hail damage on yield, as noted by Holman et al. (2023). Additionally, the damage distribution in TAI maps closely resembled the SMA maps, possibly due to the index's specific focus on the NIR area affected by the decaying wounded tissue caused by the damage. In contrast, despite being designed to capture the same feature (Peñuelas et al., 2004), the BPI index had a lower performance. This may be because the BPI was originally intended for laboratory spectrometer measurements, whose data are usually characterized by a higher signal-to-noise ratio than UAV hyperspectral values. The latter are usually more noisy, as also noted by Adão et al. (2017) and Rossiter et al. (2020), due to varying illumination conditions over the canopy, pixel spectral mixing, and UAV movements. These factors may have limited BPI's effectiveness despite noise reduction being applied during computation, since second derivatives are sensitive to small variations in the data (Rinnan et al., 2009). The TTVI index, which is similar in design to the TAI but includes an additional band at 740 nm and is mainly aimed at LAI prediction (Xing et al., 2020), yielded similar results to the TAI in capturing average differences between damages, but had a lower overall performance, failing in encompassing different dates and site conditions. Among the other tested indices, NDVI showed a poor performance. This might possibly be explained by the chlorophyll behaviour, being it not consistent

among the two years and sites and thus possibly affecting the NDVI results. In fact, the chlorophyll content in stressed vegetation does not necessarily follow a decrease pattern (Holmes, 1973; Macedo et al., 2006), and thus it might also have confounded the results obtained from other indices sensitive to chlorophyll content such as REIP (Gitelson et al., 1996) when multiple dates are considered together.

Conclusion

This study demonstrated the effectiveness of spectral mixture analysis in detecting hail damage in winter wheat and in differentiating damage intensity at both flowering and milky stages. The hail treatments affected the NIR region between 780 and 950 nm, revealing a characteristic absorbance feature associated with the presence of brown/decay pigments, which served as a viable proxy for mapping the occurrence and degree of the damage. The linear spectral unmixing technique highlighted a noticeable increase of damaged endmember abundance in accordance with damage intensity. The newly designed TAI index effectively characterized the absorbance feature and proved to be more flexible than other tested indices in handling heterogeneous conditions, such as different years and sites. Both the spectral unmixing and index analysis demonstrated promising relationships with the final yield, highlighting the link between NIR changes (e.g., brown/decay pigments) and grain output in winter wheat. However, these approaches appeared to be limited to phenological stages before winter wheat natural senescence. Therefore, it is suggested that an approach combining information from multiple indices and integrating data from weather stations could help identify the most suitable time windows for this type of analysis. Further studies are needed to assess the effectiveness of the multispectral approach across a larger dataset, including various site-specific conditions. Additionally, the TAI index response to hail damage could be tested against other plant stress factors such as droughts, pests, and diseases.

Acknowledgements This research was funded by Società Cattolica di Assicurazione. Special thanks to Lorenzo Nicoli, who supervised the damage inspection and prototype calibration, to Riccardo Polese, who helped in coordinating the field activity and the data collection, and to Lorenzo Carotta, who contributed to the design and realization of the prototype. We acknowledge the supporting activity of Archetipo s.r.l. for the UAV flights.

Funding Open access funding provided by Università degli Studi di Padova within the CRUI-CARE Agreement. This work was funded by Società Cattolica di Assicurazione S.p.A.

References

Abdelbaki, A., Schlerf, M., Retzlaff, R., Machwitz, M., Verrelst, J., & Udelhoven, T. (2021). Comparison of crop trait retrieval strategies using UAV-based VNIR hyperspectral imaging. *Remote Sensing*, *13*(9), 1–25. https://doi.org/10.3390/rs13091748.

Adão, T., Hruška, J., Pádua, L., Bessa, J., Peres, E., Morais, R., & Sousa, J. J. (2017). Hyperspectral imaging: A review on UAV-based sensors, data processing and applications for agriculture and forestry. *Remote Sensing*. https://doi.org/10.3390/rs9111110

Ahmadi, A., Joudi, M., & Janmohammadi, M. (2009). Late defoliation and wheat yield: Little evidence of post-anthesis source limitation. *Field Crops Research*, *113*(1), 90–93. https://doi.org/10.1016/j.fcr.2009.04.010.

Baret, F., & Fourty, T. (1997). Estimation of leaf water content and specific leaf weight from reflectance and transmittance measurements. *Agronomie*, *17*(9–10), 455–464. https://doi.org/10.1051/agro:19970903.

Bell, J. R., Gebremichael, E., Molthan, A. L., Schultz, L. A., Meyer, F. J., Hain, C. R., Shrestha, S., & Payne, C., K (2020). Complementing optical remote sensing with synthetic aperture radar observations of hail damage swaths to agricultural crops in the central United States. *Journal of Applied Meteorology and Climatology*, *59*(4), 665–685. https://doi.org/10.1175/JAMC-D-19-0124.1.

Bittner, S. (2006). When quinones meet amino acids: Chemical, physical and biological consequences. *Amino Acids*, *30*(3 SPEC. ISS.), 205–224. https://doi.org/10.1007/s00726-005-0298-2.

Carter, G. A. (1994). Ratios of leaf reflectances in narrow wavebands as indicators of plant stress. *International Journal of Remote Sensing*, *15*(3), 517–520. https://doi.org/10.1080/01431169408954109.

Counce, P. A., Wells, B. R., Norman, R. J., & Leong, J. (1994). Simulated hail damage to rice: II.Effects during four reproductive growth stages. *Agronomy Journal*, *86*(6), 1113–1118. https://doi.org/10.2134/agronj1994.00021962008600060035x.

Counce, P. A., Wells, B. R., & Norman, R. J. (1994a). Simulated hail damage to rice: I.Susceptible growth stages. *Agronomy Journal*, *86*(6), 1107–1113. https://doi.org/10.2134/agronj1994.00021962008600060034x.

Dal Ferro, N., Piccoli, I., Berti, A., Polese, R., & Morari, F. (2020). Organic carbon storage potential in deep agricultural soil layers: Evidence from long-term experiments in northeast Italy. *Agriculture Ecosystems and Environment*, *300*(May), 106967. https://doi.org/10.1016/j.agee.2020.106967.

Dawelbait, M., Dal Ferro, N., & Morari, F. (2017). Using landsat images and spectral mixture analysis to assess drivers of 21-Year LULC changes in Sudan. *Land Degradation and Development*, *28*(1), 116–127. https://doi.org/10.1002/ldr.2556.

De Leeuw, J., Vrieling, A., Shee, A., Atzberger, C., Hadgu, K. M., Biradar, C. M., Keah, H., & Turvey, C. (2014). The potential and uptake of remote sensing in insurance: A review. *Remote Sensing*, *6*(11), 10888–10912. https://doi.org/10.3390/rs61110888.

EnMAP-Box Developers (2019). : EnMAP-Box 3 - A QGIS Plugin to process and visualize hyperspectral remote sensing data. https://enmap-box.readthedocs.io/en/latest .

Fang, H., Baret, F., Plummer, S., & Schaepman-Strub, G. (2019). An overview of Global Leaf Area Index (LAI): Methods, products, validation, and applications. *Reviews of Geophysics*, *57*(3), 739–799. https://doi.org/10.1029/2018RG000608.

Fernandes, G. W., Oki, Y., Sanchez-Azofeifa, A., Faccion, G., & Amaro-Arruda, H. C. (2011). Hail impact on leaves and endophytes of the endemic threatened Coccoloba Cereifera (Polygonaceae). *Plant Ecology*, *212*(10), 1687–1697. https://doi.org/10.1007/s11258-011-9941-z.

Filella, I., & Peñuelas, J. (1994). The red edge position and shape as indicators of plant chlorophyll content, biomass and hydric status. *International Journal of Remote Sensing (Vol*, *15*, 1459–1470. https://doi.org/10.1080/01431169408954177.

Furlanetto, J., Dal Ferro, N., Briffaut, F., Carotta, L., Polese, R., Dramis, A., Miele, C., Persichetti, A., Nicoli, L., & Morari, F. (2021). Mapping of hailstorm and strong wind damaged crop areas using LAI estimated from multispectral imagery. *Precision Agriculture*, *'21*, 315–321. https://doi.org/10.1145/3132847.3132886.

Furlanetto, J., Dal Ferro, N., Longo, M., Sartori, L., Polese, R., Caceffo, D., Nicoli, L., & Morari, F. (2023). LAI estimation through remotely sensed NDVI following hail defoliation in maize (Zea mays L.) using Sentinel – 2 and UAV imagery. *Precision Agriculture*. https://doi.org/10.1007/s11119-023-09993-9

Gitelson, A. A., Merzlyak, M. N., & Lichtenthaler, H. K. (1996). Detection of red edge position and chlorophyll content by reflectance measurements near 700 nm. *Journal of Plant Physiology*, *148*(3–4), 501–508. https://doi.org/10.1016/S0176-1617(96)80285-9.

Gobbo, S., Ghiraldini, A., Dramis, A., Dal Ferro, N., & Morari, F. (2021). Estimation of hail damage using crop models and remote sensing. *Remote Sensing*, *13*(14), 1–13. https://doi.org/10.3390/rs13142655.

Guyot, G., & Baret, F. (1988). Utilisation de la haute resolution spectrale pour suivre l'etat des couverts vegetaux. *Journal of Chemical Information and Modeling*, *53*(9), 1689–1699.

Holman, J. D., Lollato, R. P., Zarnstorff, M., Houx, J., & Assefa, Y. (2023). Impact of simulated hail damage at different growth stages and canopy positions on rainfed and irrigated winter wheat. *Agronomy Journal*, *January 2023*. https://doi.org/10.1002/agj2.21256.

Holmes, D. P. (1973). Effects of Defoliation on Chlorophyll loss in Senescing Wheat Inflorescences and on Grain Maturation. *Canadian Journal of Plant Science*, *53*(3), 499–500. https://doi.org/10.4141/cjps73-096.

IUSS Working Group WRB. (2015). *World reference base for soil resources 2014 International soil classification system. World Soil*. Rome: FAO.

Jacquemoud, S., & Baret, F. (1990). PROSPECT: A model of leaf optical properties spectra. *Remote Sensing of Environment*, *34*(2), 75–91. https://doi.org/10.1016/0034-4257(90)90100-Z.

Lauer, J. G., Roth, G. W., & Bertram, M. G. (2004). Impact of defoliation on corn forage yield. *Agronomy Journal*, *96*(5), 1459–1463. https://doi.org/10.2134/agronj2004.1459.

Lorenz, D., Eichhorn, K., Bleiholder, H., Klose, R., Meier, U., & Weber, E. (2001). Growth stages of mono and dicotyledonous plants BBCH Monograph. *Germany: Federal Biological Research Centre for Agriculture and Forestry.*

Macedo, T. B., Peterson, R. K. D., & Weaver, D. K. (2006). Photosynthetic responses of wheat, *Triticum aestivum* L., plants to simulated insect defoliation during vegetative growth and at Grain fill. *Environmental Entomology*, *35*(6), 1702–1709. https://doi.org/10.1603/0046-225x(2006)35[1702:prowta]2.0.co;2.

Macedo, T. B., Peterson, R. K. D., Dausz, C. L., & Weaver, D. K. (2007). Photosynthetic responses of wheat, *Triticum aestivum* L., to defoliation patterns on individual leaves. *Environmental Entomology, 36*(3), 602–608. https://doi.org/10.1603/0046-225X

Mahul, O., & Stutley, C. J. (2010). Government support to agricultural insurance. In *Asia-Pacific Biotech News*, *6*(6). The World Bank. https://doi.org/10.1142/s0219030302000514.

Merzlyak, M. N., Gitelson, A. A., Chivkunova, O. B., & Rakitin, V. Y. (1999). Non-destructive optical detection of pigment changes during leaf senescence and fruit ripening. *Physiologia Plantarum*, *106*(1), 135–141. https://doi.org/10.1034/j.1399-3054.1999.106119.x.

Mohammadi, M., & Kazemi, H. (2002). Changes in peroxidase and polyphenol oxidase activities in susceptible and resistant wheat heads inoculated with Fusarium graminearum and induced resistance. *Plant Science*, *162*(4), 491–498. https://doi.org/10.1016/S0168-9452(01)00538-6.

Nicolas, J. J., Richard-Forget, F. C., Goupy, P. M., Amiot, M. J., & Aubert, S. Y. (1994). Enzymatic browning reactions in apple and apple products. *In Critical Reviews in Food Science and Nutrition, 34*(2), 109–157.

Nisi, L., Martius, O., Hering, A., Kunz, M., & Germann, U. (2016). Spatial and temporal distribution of hailstorms in the Alpine region: A long-term, high resolution, radar-based analysis. *Quarterly Journal of the Royal Meteorological Society*, *142*(697), 1590–1604. https://doi.org/10.1002/QJ.2771.

Peñuelas, J., Pinol, J., Ogaya, R., & Filella, I. (1997). Estimation of plant water concentration by the reflectance Water Index WI (R900/R970). *International Journal of Remote Sensing*, *18*(13), 2869–2875. https://doi.org/10.1080/014311697217396.

Peñuelas, J., Munné-Bosch, S., Llusià, J., & Filella, I. (2004). Leaf reflectance and photo- and antioxidant protection in field-grown summer-stressed Phillyrea Angustifolia. Optical signals of oxidative stress? *New Phytologist*, *162*(1), 115–124. https://doi.org/10.1046/j.1469-8137.2004.01007.x.

Pierpoint, W. S. (1969). o-Quinones formed in plant extracts. Their reactions with amino acids and peptides. *The Biochemical Journal*, *112*(5), 609–616. https://doi.org/10.1042/bj1120609.

Ping, J. L., & Dobermann, A. (2005). Processing of yield map data. *Precision Agriculture*, *6*(2), 193–212. https://doi.org/10.1007/s11119-005-1035-2.

Pokovai, K., & Fodor, N. (2019). Adjusting ceptometer data to improve leaf area index measurements. *Agronomy*, *9*(12), 1–13. https://doi.org/10.3390/agronomy9120866.

Proctor, C., Lu, B., & He, Y. (2017). Determining the absorption coefficients of decay pigments in decomposing monocots. *Remote Sensing of Environment*, *199*, 137–153. https://doi.org/10.1016/j.rse.2017.07.007.

Queiroz, C., Mendes Lopes, M. L., Fialho, E., & Valente-Mesquita, V. L. (2008). Polyphenol oxidase: Characteristics and mechanisms of browning control. *Food Reviews International*, *24*(4), 361–375. https://doi.org/10.1080/87559120802089332.

Richard-Forget, F. C., & Goupy, P. M. (1994). Enzymatic browning reactions in apple and apple products. *In Critical Reviews in Food Science and Nutrition*. https://doi.org/10.1080/10408399409527653

Rinnan, Å., van den Berg, F., & Engelsen, S. B. (2009). Review of the most common pre-processing techniques for near-infrared spectra. *Trends in Analytical Chemistry*, *28*(10), 1201–1222. https://doi.org/10.1016/j.trac.2009.07.007.

Rossiter, T., Furey, T., McCarthy, T., & Stengel, D. B. (2020). UAV-mounted hyperspectral mapping of intertidal macroalgae. *Estuarine Coastal and Shelf Science*, *242*(April), 106789. https://doi.org/10.1016/j.ecss.2020.106789.

Sankey, T., Donager, J., McVay, J., & Sankey, J. B. (2017). UAV lidar and hyperspectral fusion for forest monitoring in the southwestern USA. *Remote Sensing of Environment*, *195*, 30–43. https://doi.org/10.1016/j.rse.2017.04.007.

Schillaci, C., Inverardi, F., Battaglia, M. L., Perego, A., Thomason, W., & Acutis, M. (2022). Assessment of hail damages in maize using remote sensing and comparison with an insurance assessment: A case study in Lombardy. *Italian Journal of Agronomy*. https://doi.org/10.4081/ija.2022.2126

Shapiro, C. A., Peterson, T. A., & Flowerday, A. D. (1986). Yield loss due to simulated Hail damage on Corn: A comparison of actual and predicted values 1. *Agronomy Journal*, *78*(4), 585–589. https://doi.org/10.2134/agronj1986.00021962007800040006x.

Stasik, O. O., Kiriziy, D. A., Sokolosvka-Sergiienko, O. G., & Bondarenko, O. Y. (2020). Influence of drought on the photosyntethic apparatus activity, senescence rate and productivity in wheat plants. *Plant Physiology and Genetics*, *52*(5), 371–387. https://doi.org/10.15407/frg2020.05.371.

Tucker, C. (1979). Red and photographic infrared linear combinations for monitoring vegetation. *Remote Sensing of Environment*, *8*(2), 127–150.

USDA (2010). Grain loss adjustement standards handbook.

Ustin, S. L., & Jacquemoud, S. (2020). How the optical properties of leaves modifies the absorption and scattering of energy and enhance leaf functionality. In J. Cavender-Bares, J. A. Gamon, & P. A. Townsend (Eds.), *Remote sensing of plant biodiversity. In Remote Sensing of Plant Biodiversity.* Heidelberg: Springer.

Vaughn, K. C., & Duke, S. O. (1984). Function of polyphenol oxidase in higher plants. *Physiologia Plantarum*, *60*(1), 106–112. https://doi.org/10.1111/j.1399-3054.1984.tb04258.x.

Xing, N., Huang, W., Xie, Q., Shi, Y., Ye, H., Dong, Y., Wu, M., Sun, G., & Jiao, Q. (2020). A transformed triangular vegetation index for estimating winter wheat leaf area index. *Remote Sensing*, *12*(1), 1–19. https://doi.org/10.3390/RS12010016.

Yuan, N., Gong, Y., Fang, S., Liu, Y., Duan, B., Yang, K., Wu, X., & Zhu, R. (2021). Uav remote sensing estimation of rice yield based on adaptive spectral endmembers and bilinear mixing model. *Remote Sensing, 13*(11), 2190. https://doi.org/10.3390/rs13112190

Zhang, J., Cheng, T., Guo, W., Xu, X., Qiao, H., Xie, Y., & Ma, X. (2021). Leaf area index estimation model for UAV image hyperspectral data based on wavelength variable selection and machine learning methods. *Plant Methods*, *17*(1), 1–15. https://doi.org/10.1186/s13007-021-00750-5.

Zhao, J. L., Zhang, D. Y., Luo, J. H., Huang, S. L., Dong, Y. Y., & Huang, W. J. (2012). Detection and mapping of hail damage to corn using domestic remotely sensed data in China. *Australian Journal of Crop Science*, *6*(1), 101–108.

Zhou, J., Pavek, M. J., Shelton, S. C., Holden, Z. J., & Sankaran, S. (2016). Aerial multispectral imaging for crop hail damage assessment in potato. *Computers and Electronics in Agriculture*, *127*, 406–412. https://doi.org/10.1016/j.compag.2016.06.019.

Zhu, G. X., Midmore, D. J., Radford, B. J., & Yule, D. F. (2004). Effect of timing of defoliation on wheat (*Triticum aestivum*) in central Queensland: 1. Crop response and yield. *Field Crops Research, 88*(2–3), 211–226. https://doi.org/10.1016/j.fcr.2004.01.014